SHOULD HYDRODYNAMICS BE TAKEN INTO ACCOUNT WHEN CALCULATING THE GROWTH RATE OF MICROALGAE IN A PHOTOBIOREACTOR?

J. IGNACIO FIERRO U., LIU-DI LU, OLIVIER BERNARD

Abstract. Microalgae are photosynthetic organisms cultivated in photobioreactors, where light intensity is one of the most important factors affecting their growth rate. At lower intensity, the microalgae are photolimited, since the amount of photons they received is not enough to optimally trigger the photosynthetic machinery. On the other hand, higher intensity induces damage in key proteins within the photosynthetic center of the cells. Due to the mixing in the photobioreactor, which creates a strong light gradient, the growth of the cells is affected by their light exposure history, which results from the hydrodynamics of the photobioreactor. We use the mechanistic model of Han to capture both photoinhibition and photolimitation. First, we compute the time-averaged growth rate for arbitrary continuous light signals. Our analysis reveals how mixing influences the average growth rate, assuming that hydrodynamics generate periodic light signals. Then, we tackle the challenge of computing the growth rate in photobioreactors simulated through computational fluid dynamics, considering a single-phase incompressible fluid. We conclude by examining the case of the raceway pond, and assess the error resulting from various approximations of the growth rate.

1. Introduction. Microalgae are able to convert CO_2 into biomass using energy from visible light. They are cultivated in photobioreactors, which exhibit two noteworthy characteristics. Firstly, the cells are light absorbing particles, which lead to a heterogeneous light distribution within the reactor. Zones near the light source experience intense illumination, while areas in deeper layers are in the dark. Secondly, the photobioreactor is intensively mixed to avoid biomass sedimentation and spatial heterogeneity of the nutrients. As a result, cells are advected through a light gradient, so that they perceive a succession of high and low light intensities. Photon harvesting in microalgae is a dynamic process, and the average growth rate within a photobioreactor results from this complex interplay between photosystem dynamics and hydrodynamics [5]. Accounting for such a complex interaction is a challenging problem, requiring accurate representation of both the hydrodynamics within the reactor and the dynamics of photon harvesting in response to light variations. This approach, which explicitly considers the light history of the cells, was classified as type III in [3]. However, such models are often too complex for practical application, leading to simplified computations of the growth rate μ. In the type I models, μ depends only on the incident light impinging the reactor. The type II models, account for light gradients in the culture, usually coupling the Beer–Lambert law to represent the light gradient, with a Monod-like or Haldane-type function for $\mu(I)$. Both type I and type II models are *static*, while type III models are *dynamic*.

Photosystem dynamics are generally represented by three-population models, such as the Han model [9] or the Eilers–Peeters model [6]. They consist of three differential equations where each state variable represents the probability of the photosystem to be in one of three states: open and ready to process photons, closed and busy processing photons, or damaged due to excess light energy. These models capture two phenomena: photoabsorption and photoinhibition, which occur on different timescales. The damaged rate is considerably slower than the photon harvesting process. The difference of the timescales induces a slow-fast approximation in the

three-population model [10].

When a cell is advected in a photobioreactor, it perceives a continuous light signal over time. Using the Han model, we will study the influence of this fluctuating signal on the growth rate. Taking into account the typical timescale of light variations, we will simplify the Han model using a slow-fast approximation. Then, we will compare the outcome of this simplified Han model with predictions when assuming the photosystems are in a steady state. Our calculations will first be applied to simple periodic light signals, and then to realistic light patterns derived from computational fluid dynamics simulations (CFD) in a specific photobioreactor, a raceway system, where mixing is carried out by a paddle wheel.

This paper is organized as follows: in Section 2 we present the basis of the Han model. We define two strategies for computing the growth rate: μ_A accounts for the dynamics of the photosystem, and μ_S assumes a static response. We write an explicit relation between the two functions, and present one of the main results of this paper, which establishes the relationship between the time-averaged dynamic growth rate (μ_A) and the static growth rate (μ_S). In Section 3.3, we study continuous periodic light signals and show that all solutions of the Han model converge to a unique periodic solution. We give the exact average growth rate for any continuous periodic light signal, and simulate the mixing in a photobioreactor using two specific cases. Finally, in Section 2.2 we analyze the raceway pond, where we use a CFD model to simulate the motion of particles within the photobioreactor, tracking the light perceived by individual microalgae. We compare the two growth rate functions, and refine the average growth rate computation to take into account the spatial component. We conclude by demonstrating a close relation between the hydrodynamics and the average growth rate.

2. Biological and hydrodynamic models.

2.1. Biological model. We consider the mechanistic model of Han [9] which characterizes the photoinhibition induced by the photodamage of the photosystem II (PSII). There are three possible states for the PSII: open or reactive state A, closed or activated state B, and inhibited or damaged state C. The dynamics of PSII can be described by the differential equations:

(2.1)
$$\begin{aligned}
\frac{\mathrm{d}A}{\mathrm{d}t} &= -I\sigma_P A + \frac{B}{\tau}, \\
\frac{\mathrm{d}B}{\mathrm{d}t} &= I\sigma_P A - \frac{B}{\tau} + k_r C - k_d \sigma_P I B, \\
\frac{\mathrm{d}C}{\mathrm{d}t} &= -k_r C + k_d \sigma_P I B,
\end{aligned}$$

where σ_P ($\mu\mathrm{mol}^{-1}\mathrm{m}^2$) is the effective cross-section of the PSII, I ($\mu\mathrm{mol}\,\mathrm{m}^{-2}\mathrm{s}^{-1}$) is the light intensity perceived by the microalgae starting from 0, τ (s) is the minimal time required for an electron to transfer from water on the donor side of the photosynthetic unit to the terminal electron acceptors, which is also called the turnover time, k_d ($-$) is the damage rate and k_r (s^{-1}) is the recovery rate of the PSII. A, B and C represent the probability distribution of each state such that

(2.2) $$A + B + C = 1.$$

The algal growth rate is assumed to be proportional to the open state A and the light intensity I. More precisely, the growth rate given by the kinetic model (2.1)

2

90 corresponds to

91 (2.3)
$$\mu_A(I, A) := \alpha \sigma_P I A,$$

92 where α $(-)$ is a constant of proportionality. At steady state, the state A of the
93 system (2.1) tends towards A_S (see, e.g., [5]). This corresponds exactly to a Haldane
94 model where the growth rate is a function of light, that is

95 (2.4)
$$\mu_S(I) = \alpha \sigma_P I A_S = \alpha \sigma_P I \frac{1}{1 + \tau \sigma_P I + \frac{k_d}{k_r} \tau (\sigma_P I)^2}.$$

96 The maximum of μ_S is given by

97
$$\mu_{\max} = \frac{\alpha}{\tau + 2\sqrt{\frac{k_d}{k_r} \tau}},$$

98 and it is reached when the light intensity value is

99 (2.5)
$$I_{\mathrm{opt}} = \frac{1}{\sigma_P \sqrt{\frac{k_d}{k_r} \tau}}.$$

100 As shown in [7], using (2.2) and substituting it into the system (2.1), we end up with
101 two equations

102 (2.6)
$$\frac{\mathrm{d}A}{\mathrm{d}t} = -\left(\sigma_P I + \frac{1}{\tau}\right) A - \frac{1}{\tau} C + \frac{1}{\tau},$$
$$\frac{\mathrm{d}C}{\mathrm{d}t} = \varepsilon \left[-\sigma_P I A - \left(\sigma_P I + \frac{k_r}{k_d}\right) C + \sigma_P I \right],$$

103 which has slow/fast timescales due to the presence of the factor $\varepsilon = k_d$. In this case,
104 we can consider the slow manifold proposed in [13]

105 (2.7)
$$A = \frac{1 - C}{1 + \tau \sigma_P I},$$

106 and reduce the system (2.6) to a single equation for C

107 (2.8)
$$\frac{\mathrm{d}C}{\mathrm{d}t} = -(\gamma(I) + k_r) C + \gamma(I),$$

108 with $\gamma(I) := \frac{k_d \tau (\sigma_P I)^2}{1 + \tau \sigma_P I}$. In particular, the steady state of C is given by

109
$$C_S := \frac{\gamma(I)}{\gamma(I) + k_r} = \frac{\frac{k_d}{k_r} \tau (\sigma_P I)^2}{1 + \tau \sigma_P I + \frac{k_d}{k_r} \tau (\sigma_P I)^2}.$$

110 Consequently, the steady state of A can be obtained by substituting C_S into (2.7).
111 For a continuous bounded light signal $I : [0, +\infty) \to [I_{\min}, I_{\max}]$, $0 \leq I_{\min} \leq$
112 $I_{\max}$, we present an estimation of the growth rate μ_A as a function of the static
113 growth rate μ_S. To simplify the notations, we write in the following $\mu_A(t)$ instead
114 of $\mu_A(I(t), A(A(0); t))$ and $\mu_S(t)$ instead of $\mu_S(I(t))$. We show next that the initial
115 condition can be neglected.

3

116 PROPOSITION 2.1. *Let $I : [0, +\infty) \to [I_{\min}, I_{\max}]$ be a continuous bounded light*
117 *signal. Assuming that $A(0) = 0$, the growth rate μ_A can be written as*

118 (2.9)
$$\mu_A(t) = \mu_S(t)(\gamma(I(t)) + k_r) \int_0^t e^{-\int_s^t \gamma(I(w)) + k_r \, \mathrm{d}w} \, \mathrm{d}s.$$

119 *Furthermore, the following estimations hold*

120 (2.10)
$$\mu_S(t)\frac{\gamma(I(t)) + k_r}{\gamma(I_{\max}) + k_r} \left(1 - e^{-(\gamma(I_{\max}) + k_r)t}\right) \le \mu_A(t) \le \mu_S(t)\frac{\gamma(I(t)) + k_r}{\gamma(I_{\min}) + k_r}.$$

121 In general, for any initial condition $A(0) = A_0$, the associated growth rate converges
122 to (2.9) when t goes to infinity.

123 *Proof.* The general solution of (2.8) is given by

124 (2.11)
$$C(t) = C(0)e^{-\int_0^t \gamma(I(w)) + k_r \, \mathrm{d}w} + \int_0^t \gamma(I(s))e^{-\int_s^t \gamma(I(w)) + k_r \, \mathrm{d}w} \, \mathrm{d}s.$$

125 Using then (2.7), A can be written as

$$A(A(0); t) = A(0)\frac{1 + \tau\sigma_P I(0)}{1 + \tau\sigma_P I(t)}e^{-\int_0^t \gamma(I(w)) + k_r \, \mathrm{d}w}$$

126 (2.12)
$$+ A_S(t)(\gamma(I(t)) + k_r)\int_0^t e^{-\int_s^t \gamma(I(w)) + k_r \, \mathrm{d}w} \, \mathrm{d}s,$$

127 which depends on the initial value $A(0)$. If $A(0) = 0$, equation (2.12) becomes,

128 (2.13)
$$A(0; t) = A_S(t)(\gamma(I(t)) + k_r)\int_0^t e^{-\int_s^t \gamma(I(w)) + k_r \mathrm{d}w} \, \mathrm{d}s.$$

129 Equation (2.9) is deduced from the definitions (2.3) and (2.4). The upper bound in
130 (2.10) follows from the fact that γ is an increasing function of I and

131
$$\int_0^t e^{-\int_s^t \gamma(I(w)) + k_r \, \mathrm{d}w} \, \mathrm{d}s \le \int_0^t e^{-\int_s^t \gamma(I_{\min}) + k_r \, \mathrm{d}w} \, \mathrm{d}s = \frac{1 - e^{-(\gamma(I_{\min}) + k_r)t}}{\gamma(I_{\min}) + k_r}$$
$$\le \frac{1}{\gamma(I_{\min}) + k_r}.$$

132 For a similar reason, we find

133
$$\int_0^t e^{-\int_s^t \gamma(I(w)) + k_r \, \mathrm{d}w} \, \mathrm{d}s \ge \int_0^t e^{-\int_s^t \gamma(I_{\max}) + k_r \, \mathrm{d}w} \, \mathrm{d}s = \frac{1 - e^{-(\gamma(I_{\max}) + k_r)t}}{\gamma(I_{\max}) + k_r}.$$

134 Substituting these two inequalities into (2.13) and using again the definitions (2.3)
135 and (2.4), we obtain the estimation (2.10). Finally, if $A(0) = A_0 \ne 0$, using (2.12)
136 and (2.13), we have

$$|A(A(0); t) - A(0; t)| = |A(0)|\frac{1 + \tau\sigma_P I(0)}{1 + \tau\sigma_P I(t)}e^{-\int_0^t \gamma(I(w)) + k_r \, \mathrm{d}w}$$

137 (2.14)
$$\le |A(0)|\frac{1 + \tau\sigma_P I_{\max}}{1 + \tau\sigma_P I_{\min}}e^{-\int_0^t \gamma(I(w)) + k_r \, \mathrm{d}w}$$
$$\le |A(0)|\frac{1 + \tau\sigma_P I_{\max}}{1 + \tau\sigma_P I_{\min}}e^{-k_r t}.$$

138 The latter converges to zero when t goes to infinity, thus $A(A(0); t)$ converges to
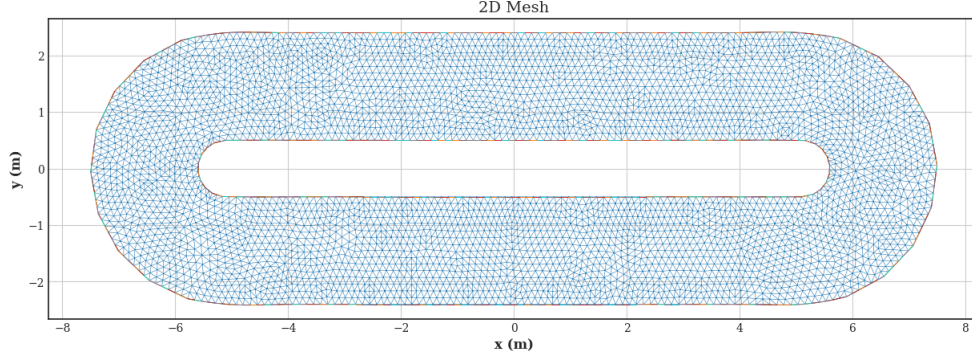139 $A(0; t)$. $\square$

4

Fig. 2.1: 2D mesh of the simulated raceway pond.

140 Based on Proposition 2.1, for large timescale, we will assume that the initial
141 condition of the state A is zero.

142 **2.2. Computational fluid dynamic model.** The water flow in a raceway pond
143 can be simulated with CFD, which integrates the Navier–Stokes equations. Several
144 studies have used CFD to simulate the velocity field in open ponds [16, 17]. Lagrangian
145 approaches have also been used to assess the mixing efficiency in algae cultures. For
146 example, in [1], the mixing length is computed as a result of different paddle wheel
147 velocities. Here, we use a 2D triangular mesh representing a real raceway pond from
148 the Environmental Biotechnology Laboratory of INRAE Narbonne, France [12] (See
149 Figure 2.1). The third dimension is given by the discretization of the free surface
150 following the model in [2].

151 **2.3. Hydrodynamics and cell tracking.** A layer-averaged Euler and Navier–
152 Stokes model for the numerical simulation of incompressible free surface is presented
153 in [2]. The multi-layered model corresponds to a Galerkin type approximation. The
154 system is solved using a fixed 2D mesh of the bottom of the raceway and the lay-
155 ers are defined by the water depth, giving the third dimension of the system. The
156 incompressible and hydrostatic Navier–Stokes system with free surface is given by

$$\nabla \mathbf{U} = \mathbf{F},$$

157 (2.15)
$$\frac{\partial \mathbf{u}}{\partial t} + \nabla_{x,y}(\mathbf{u} \otimes \mathbf{u}) + \frac{\partial \mathbf{u}w}{\partial z} = \frac{1}{\rho_0} \nabla_{x,y}\sigma + \frac{\mu}{\rho_0} \frac{\partial^2 \mathbf{u}}{\partial z^2},$$

$$\frac{\partial p}{\partial z} = -\rho_0 g,$$

158 where $\mathbf{U} = (u, v, w)^T$ is the velocity of the liquid, $\mathbf{u} = (u, v)^T$ is the horizontal velocity,
159 σ is $-pI_d + \Sigma$, where $\Sigma = \mu\nabla_{x,y}\mathbf{u}$ is the total stress tensor, p is the pressure, g is the
160 gravity acceleration constant, ρ_0 is the fluid density and μ is the viscosity coefficient.
161 The fluid is assumed to be Newtonian. The paddle wheel is modelled by the force $\mathbf{F}$
162 [4] given by

163 (2.16)
$$\mathbf{F} = F\left(\sqrt{(x - x_{\text{wheel}})^2 + (z - z_{\text{wheel}})^2}\omega\right)^2 \begin{pmatrix} \cos(\theta) \\ 0 \\ \sin(\theta) \end{pmatrix},$$

5

Time: 73.6 s

Velocity Magnitude (m/s)

0   0.1   0.2   0.3   0.4   0.5   0.6   0.7   0.8   0.9   1
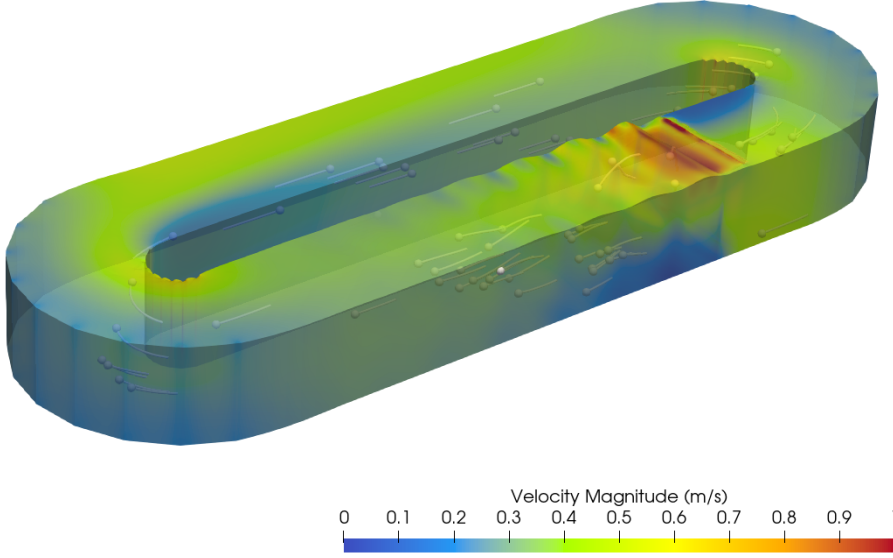
Fig. 2.2: Representation of the raceway and the velocity field with some particles obtained from the CFD simulations. The height correspond to $0.3(m)$ and it is scaled with a factor of 5 to have a better visualization. The paddle wheel simulated in this image works at 20 RPM (rounds per minute).

where F is a constant, θ is the angle between the vertical axis and the blade and $\omega = \dot{\theta}$, and x_{wheel}, z_{wheel} are the coordinates of the paddle wheel in the x and z axis respectively. Note that the force does not affect the y-axis, which is parallel to the central axis of the paddle wheel. It has been shown in [4] the computational efficiency of simulating a raceway pond using such model (2.15)-(2.16).

Lagrangian's trajectories of several particles can be reconstructed from the Eulerian description (2.15) denoted by $(\mathbf{X}_n)_{i=1}^{N_{par}}$, where N_{par} is the number of simulated particles. The position of each particle $\mathbf{X}_n(t) = (x_n, y_n, z_n)^T$ is computed by solving the equation

(2.17)
$$\frac{d\mathbf{X}_n(t)}{dt} = \mathbf{U}(t),$$
$$\mathbf{X}_n(0) = (x_{n0}, y_{n0}, z_{n0})^T,$$

where (x_{n0}, y_{n0}, z_{n0}) is the initial position of the particle. We denote by Ω the domain of the raceway. We initiate the position of the particles randomly, following a uniform distribution in the domain Ω.

The CFD model was already validated using a Pulsed Ultrasonic Doppler Velocimetry [12]. Other similar works based on the same pond [11, 15] have considered a growth model tracking the position of Lagrangian trajectories, using the same model (2.15)–(2.17). Figure 2.2 shows the distribution of the velocity magnitude in the simulated raceway pond and the streamlines after 10 minutes of simulations. The paddle wheel is positioned just above the red surface. Some cells (in white) are represented together with their respective streamlines. The trajectories of the cells are
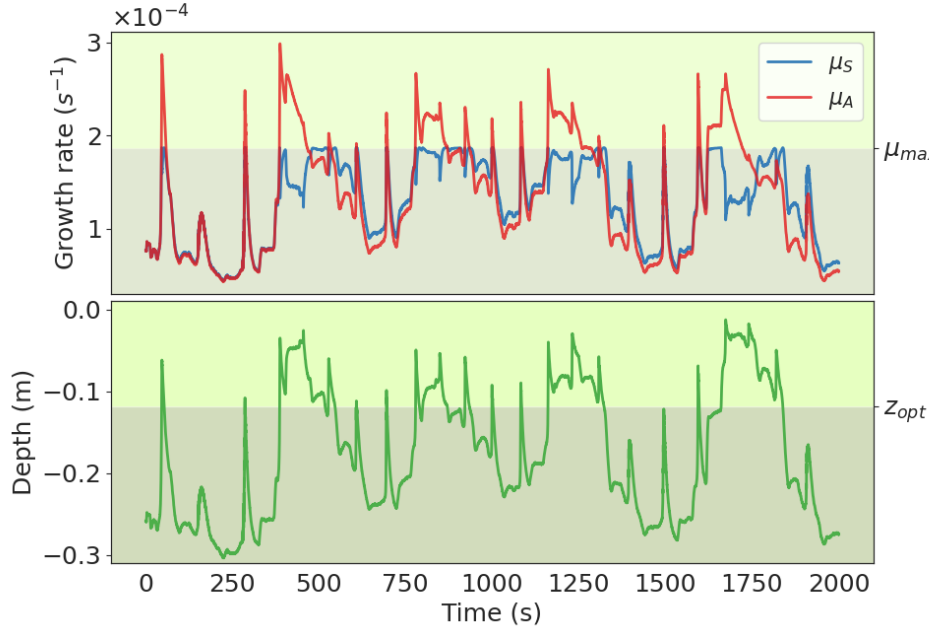
6

Fig. 2.3: Actual growth rate μ_A and static approximation μ_S for a simulated trajectory in the raceway operated at 20 RPM with an initial height of water equal to $0.3(m)$. The maximum value of the function μ_S is denoted by $\mu_{\max}$ and the depth at which this value is reached by z_{opt}.

mainly horizontal in the straight sections of the raceway pond. The fluid domain along the z-axis is delimited by the free surface denoted by $\eta(t, x, y)$, then the system (2.15) is completed with the following boundary condition:

$$\frac{\partial \eta}{\partial t} \mathbf{u} \cdot \nabla_{x,y} \eta = 0.$$

For more details of the hydrodynamic model, we refer to [2].

2.4. Light distribution within the raceway pond. We assume that the light arrives perpendicular to the ground surface. The light reaching a cell $\mathbf{X}_n$ travels a distance $\eta(t, x_n, y_n) - z_n$, from the free surface to the position of the cell. Then the light signal I_n perceived by this particle is computed with the Beer-Lambert law as

$$(2.18) \qquad I_n(t) = I_0 e^{-\xi(\eta(t,x_n,y_n)-z_n)},$$

where I_0 is the light perceived at the free surface, $\xi > 0$ is the light extinction constant.

Figure 2.3 shows the tracking of a single cell within the raceway pond. We distinguish two areas within the photobioreactor: the photoinhibited section (light green), where the light perceived is greater than the optimal light I_{opt} defined in (2.5), and the photolimited section (dark green), where the light perceived is lower than I_{opt}. We denote by z_{opt} the optimal depth which corresponds to the depth at which the

7

algae perceive the light I_{opt} given by

$$z_{\mathrm{opt}} = \frac{1}{\xi} \ln \left(\frac{I_0}{I_{\mathrm{opt}}} \right).$$

When the particle travels from the photolimited area to the photoinhibited area, crossing z_{opt}, the difference between μ_S and μ_A is more observable. This occurs when the particle moves faster in the z-axis than the photoinhibition mechanism. In this case, the growth rate μ_A could reach larger values than the predicted one with μ_S. When the cell does not go through this section fast enough, then μ_S can accurately approximate μ_A.

2.5. Growth rate in the raceway pond. To estimate the growth rate in the raceway pond, we need to define the average growth rate of all simulated particles moving within the photobioreactor. We first define the time-averaged dynamic growth rate and static growth rate by

(2.19) $$\overline{\mu}_A := \frac{1}{T} \int_0^T \mu_A(t) \, \mathrm{d}t, \quad \overline{\mu}_S := \frac{1}{T} \int_0^T \mu_S(t) \, \mathrm{d}t.$$

Then the space-time-averaged dynamic growth rate and static growth rate are defined as

(2.20) $$\overline{\overline{\mu}}_A = \frac{1}{N_{par}} \sum_{n=1}^{N_{par}} \overline{\mu}_A(I_n), \quad \overline{\overline{\mu}}_S = \frac{1}{N_{par}} \sum_{n=1}^{N_{par}} \overline{\mu}_S(I_n).$$

In the Eulerian description, the static growth rate μ_S can be computed for each point in the raceway domain Ω. At each point $(x, y, z) \in \Omega$, the perceived light is computed using (2.18) as $I(x, y, z) = I_0 e^{-\xi(\eta(t,x,y)-z)}$, and the volume-averaged growth rate can be defined by

$$\overline{\mu}_\Omega = \frac{1}{V(\Omega)} \int_\Omega \mu_S(I(x, y, z)) \, \mathrm{d}x\mathrm{d}y\mathrm{d}z,$$

where $V(\Omega)$ is the volume of the raceway.

3. Formal analysis of the average growth rate.

3.1. Time-averaged growth rate. We first show the relation between two time-averaged growth rate $\overline{\mu}_A$ and $\overline{\mu}_S$ defined in (2.19).

THEOREM 3.1. *Let I be a bounded continuous light signal perceived by a single cell. Assuming that $A(0) = 0$, for a given time period T, the time-averaged dynamics growth rate $\overline{\mu}_A$ can be written as a function of the time-averaged static growth rate $\overline{\mu}_S$ via*

(3.1) $$\overline{\mu}_A = \overline{\mu}_S + \overline{\mu}_H + \mathcal{O}(1/T),$$

where

(3.2) $$\overline{\mu}_H := \frac{1}{T} \int_0^T \frac{\mathrm{d}\mu_S(t)}{\mathrm{d}t} \phi(t) \, \mathrm{d}t, \quad \phi(t) := \int_0^t e^{-\int_s^t \gamma(I(w))+k_r \, \mathrm{d}w} \, \mathrm{d}s,$$

and $\mathcal{O}(1/T) = -\frac{\mu_S(T)}{T} \phi(T)$ which goes to zero when $T \to +\infty$.

8

Interpretation of Theorem 3.1: In a system mainly laminar, where cells stay at a constant depth (or are slowly advected vertically), for which the dynamical component of the growth rate $\overline{\mu}_H$ is negligible, the average growth rate over a sufficiently long time period T can be accurately computed using the static approximation $\overline{\mu}_S$ based on the Haldane model. In a system with high velocities in the direction of the light gradient, this approximation must be refined.

Proof. Using (2.9) and integration by parts, we find

$$\int_0^T \mu_A(t)\mathrm{d}t = \int_0^T \mu_S(t)(\gamma(I(t)) + k_r) \int_0^t e^{-\int_s^t \gamma(I(w)) + k_r\, \mathrm{d}w}\, \mathrm{d}s\mathrm{d}t$$

$$= \int_0^T \int_s^T \mu_S(t)(\gamma(I(t)) + k_r)e^{-\int_s^t \gamma(I(w)) + k_r\, \mathrm{d}w}\, \mathrm{d}t\mathrm{d}s$$

$$= -\int_0^T \int_s^T \mu_S(t)\frac{\mathrm{d}}{\mathrm{d}t}\left(e^{-\int_s^t \gamma(I(w)) + k_r\, \mathrm{d}w}\right)\, \mathrm{d}t\mathrm{d}s$$

$$= \int_0^T \mu_S(s) - \mu_S(T)e^{-\int_s^T \gamma(I(w)) + k_r\, \mathrm{d}w}\, \mathrm{d}s$$

$$+ \int_0^T \int_s^T \frac{\mathrm{d}\mu_S(t)}{\mathrm{d}t}e^{-\int_s^t \gamma(I(w)) + k_r\, \mathrm{d}w}\, \mathrm{d}t\mathrm{d}s.$$

Dividing the latter by T, we get (3.1). Moreover, for a given time period T, the function ϕ defined in (3.2) can be upper bounded by

(3.3) $$\phi(T) \leq \int_0^T e^{-(\gamma(I_{\min}) + k_r)(T-s)}\, \mathrm{d}s = \frac{1 - e^{-(\gamma(I_{\min}) + k_r)T}}{\gamma(I_{\min}) + k_r},$$

and lower bounded by

(3.4) $$\phi(T) \geq \int_0^T e^{-(\gamma(I_{\max}) + k_r)(T-s)}\, \mathrm{d}s = \frac{1 - e^{-(\gamma(I_{\max}) + k_r)T}}{\gamma(I_{\max}) + k_r}.$$

This reveals the fact that $\mathcal{O}(1/T) \to 0$ as $T \to \infty$. $\qquad\square$

Note that

$$|\mathcal{O}(1/T)| \leq \frac{\mu_{\max}}{T}\frac{1}{\gamma(I_{\min}) + k_r} \leq \frac{\mu_{\max}}{T}\frac{1}{k_r}.$$

Then, for $T \gg 1/k_r$, we can approximate $\overline{\mu}_A$ with

$$\overline{\mu}_A \approx \overline{\mu}_S + \overline{\mu}_H,$$

where $\overline{\mu}_H$ is defined in (3.2). The quantity $1/k_r$ corresponds to the time needed to go from the state C to B in the Han model, and $T \gg 1/k_r$ means that the period T must be large enough to incorporate the effect of the recovery.

3.2. Space-time-averaged growth rate. We discuss here how the hydrodynamics of the raceway pond affects the growth rate $\overline{\overline{\mu}}_A$ defined in (2.20).

PROPOSITION 3.2. *The space-time-averaged dynamic growth rate can be bounded by the average velocity in the z-axis v_z as*

(3.5) $$\overline{\overline{\mu}}_A \leq \overline{\overline{\mu}}_S + \frac{\alpha\xi\sigma_P I_0}{k_r}\frac{1}{N_{par}}\sum_{n=1}^{N_{par}} \frac{1}{T}\int_0^T |v_z(t, \boldsymbol{X}_n)|\, \mathrm{d}t + \frac{\mu_{\max}}{Tk_r}.$$

9

Proof. For each particle $\mathbf{X}_n$ and its perceived light signal I_n, we have

$$|\overline{\mu}_A(I_n)| \leq \frac{1}{T} \int_0^T \left| \frac{\mathrm{d}\mu_S(I_n(t))}{\mathrm{d}t} \right| \phi(I_n(t)) \, \mathrm{d}t = \frac{1}{T} \int_0^T \left| \frac{\mathrm{d}\mu_S(I_n(t))}{\mathrm{d}I_n} \frac{\mathrm{d}I_n(t)}{\mathrm{d}t} \right| \phi(I_n(t)) \, \mathrm{d}t.$$

Using then the inequality (3.3), we obtain

$$|\overline{\mu}_A(I_n)| \leq \frac{1}{T} \int_0^T \left| \frac{\mathrm{d}\mu_S(I_n(t))}{\mathrm{d}I_n} \frac{\mathrm{d}I_n(t)}{\mathrm{d}t} \right| \frac{(1 - e^{-(\gamma(I_{n,\min}+k_r)t)})}{\gamma(I_{n,\min}) + k_r} \, \mathrm{d}t,$$

$$\leq \frac{1}{T(\gamma(I_{n,\min}) + k_r)} \int_0^T \left| \frac{\mathrm{d}\mu_S(I_n(t))}{\mathrm{d}I_n} \frac{\mathrm{d}I_n(t)}{\mathrm{d}t} \right| \, \mathrm{d}t,$$

$$\leq \frac{1}{Tk_r} \int_0^T \left| \frac{\mathrm{d}\mu_S(I_n(t))}{\mathrm{d}I_n} \frac{\mathrm{d}I_n(t)}{\mathrm{d}t} \right| \, \mathrm{d}t,$$

where $I_{n,\min}$ is the minimum value of I_n in the interval $[0, T]$. Note that from the Beer–Lambert law, we have $\frac{\mathrm{d}}{\mathrm{d}t} I_n(t) = -\xi I_n v_z(t, \mathbf{X}_n)$, with v_z the velocity in the z-axis of the raceway pond. It follows that

$$|\overline{\mu}_A(I_n)| \leq \frac{\xi}{Tk_r} \int_0^T \left| \frac{\mathrm{d}\mu_S(I_n(t))}{\mathrm{d}I_n} I_n(t) v_z(t, \mathbf{X}_n) \right| \, \mathrm{d}t.$$

Furthermore, we have $\max_{I \geq 0} \frac{\mathrm{d}}{\mathrm{d}I} \mu_S(I) = \alpha \sigma_P$, and $I_n(t) \leq I_0$, then

$$|\overline{\mu}_A(I_n)| \leq \frac{\alpha \xi \sigma_P I_0}{Tk_r} \int_0^T |v_z(t, \mathbf{X}_n)| \, \mathrm{d}t.$$

Using Equation (3.1):

$$\overline{\overline{\mu}}_A = \overline{\overline{\mu}}_S + \frac{1}{N_{par}} \sum_{n=1}^{N_{par}} \overline{\mu}_H(I_n) - \frac{\mu_S(I_n(t))}{T} \phi(I_n(t)),$$

$$\leq \overline{\overline{\mu}}_S + \frac{1}{N_{par}} \sum_{n=1}^{N_{par}} |\overline{\mu}_H(I_n)| + \frac{\mu_S(I_n(t))}{T} \phi(I_n(t)),$$

$$\leq \overline{\overline{\mu}}_S + \frac{1}{N_{par}} \sum_{n=1}^{N_{par}} \frac{\alpha \xi \sigma_P I_0}{Tk_r} \int_0^T |v_z(t, \mathbf{X}_n)| \, \mathrm{d}t + \frac{\mu_{\max}}{Tk_r},$$

which proves the inequality (3.5). $\qquad\square$

Interpretation of Proposition 3.2: We can ignore the term $\mu_{\max}/T$ in (3.5) when the time period T is large enough. Then, the difference between the space-time-averaged growth rate $\overline{\overline{\mu}}_A$ and $\overline{\overline{\mu}}_S$ cannot be bigger than

$$\frac{\alpha \xi \sigma_P I_0}{k_r} \overline{|v_z|} \quad \text{with} \quad \overline{|v_z|} = \frac{1}{N_{par}} \sum_{n=1}^{N_{par}} \int_0^T |v_z(t, \mathbf{X}_n)| \, \mathrm{d}t.$$

Here, $\overline{|v_z|}$ is an indicator of how mixed is the photobioreactor in the z-axis. A non-mixed photobioreactor will have $\overline{|v_z|} = 0$, showing no difference between $\overline{\overline{\mu}}_S$ and $\overline{\overline{\mu}}_A$. Also, the value of the light extinction ξ plays an important role, where lower values of this parameter present less variations of the light gradient inside the reactor.

10

3.3. Periodic light signals. When the light signal is periodic, we can be more accurate in the results presented in Theorem 3.1. Let T now be the period of the continuous light signal I perceived by the cell, we have the following result.

PROPOSITION 3.3. *Let I a continuous periodic function, i.e., $I(t+T) = I(t)$ $\forall t \in [0, +\infty)$. Then, all solutions of* (2.8) *converge to a unique periodic solution.*

Proof. The periodic solution C_p is obtained by imposing $C_p(T) = C_p(0)$ in (2.11), and we find

$$C_p(0) = \frac{\int_0^T \gamma(I(s))e^{-\int_s^T \gamma(I(w))+k_r\,\mathrm{d}w}\,\mathrm{d}s}{1 - e^{-\int_0^T \gamma(I(w))+k_r\,\mathrm{d}w}}.$$

Let C be a solution of (2.8) and $\varepsilon = C - C_p$, we have

$$\dot{\varepsilon} = -(\gamma(I) + k_r)\varepsilon.$$

The solution is given by

$$\varepsilon(t) = \varepsilon(0)e^{-\int_0^t \gamma(I(s))\,\mathrm{d}s}e^{-k_r t},$$

which can be bounded by

$$|\varepsilon(t)| \leq |\varepsilon(0)|e^{-(\gamma(I_{\min})+k_r)t}.$$

Then ε goes to zero as $t \to \infty$. $\qquad\square$

PROPOSITION 3.4 (Dynamic growth rate for periodic signal). *Let us consider a continuous periodic light signal I of period T, i.e., $I(T) = I(0)$. Then the dynamic growth rate μ_A associated with the only periodic solution C_p is given by:*

(3.6)
$$\mu_A(t) = \mu_S(t)(\gamma(I(t)) + k_r)\left[\phi(t) + \frac{\phi(T)O(T)}{1 - O(T)}\right].$$

where ϕ is given by (3.2) *and $O(T) = e^{-\int_0^T \gamma(I(w))+k_r\,\mathrm{d}w}$.*

Proof. From (2.12), we have

$$\mu_A(T) = \mu_S(T)(\gamma(I(t)) + k_r)\phi(T) + \mu_A(0)\frac{I(T)}{I(0)}\frac{1 + \tau\sigma_P I(0)}{1 + \tau\sigma_P I(T)}e^{-\int_0^T \gamma(I(w))+k_r\,\mathrm{d}w}.$$

As the function I is periodic $I(T) = I(0)$, then $C_p(0) = C_p(T)$, and the growth rate is also periodic. Imposing $\mu_A(T) = \mu_A(0)$, we can obtain its value as:

$$\mu_A(T) = \mu_S(T)(\gamma(I(t)) + k_r)\phi(T) + \mu_A(T)e^{-\int_0^T \gamma(I(w))+k_r\,\mathrm{d}w},$$

and thus

$$\mu_A(T) = \mu_S(T)\frac{(\gamma(I(t)) + k_r)\phi(T)}{1 - e^{-\int_0^T \gamma(I(w))+k_r\,\mathrm{d}w}}.$$

Substituting then into (2.9), we find (3.6). $\qquad\square$

In the same way, we obtain the following result for the time-averaged dynamic growth rate in the periodic case.

11

THEOREM 3.5 (Time-averaged growth rate in the periodic case).   *Considering a periodic light signal I of period T. The time-averaged dynamic growth rate $\overline{\mu}_A$ is given by:*

(3.7)
$$\overline{\mu}_A = \overline{\mu}_S + \frac{1}{1 - O(T)} \left[\overline{\mu}_H + \frac{O(T)}{T} \int_0^T \phi(T) - \phi(t) \, \mathrm{d}t \right].$$

Interpretation of Theorem 3.5: this theorem clarifies the results of Theorem 3.1, and better characterizes the dynamical component of the growth rate $\overline{\mu}_H$ which must be added to the static approximation $\overline{\mu}_S$ when the velocities along the light gradient are marked.

Proof. The proof follows the same steps as in theorem 3.1 using the dynamic growth rate computed in the periodic case (3.6). □

Note that, when T is large enough, meaning that $T \gg 1/k_r$, $O(T) \to 0$, leading again to the same approximation in the non-periodic case, i.e., $\overline{\mu}_A \approx \overline{\mu}_S + \overline{\mu}_H$.

3.4. Characterization of the dynamical component $\overline{\mu}_H$ as a function of the light regime. We have already seen that the time-averaged dynamic growth rate can be approximated by $\overline{\mu}_A \approx \overline{\mu}_S + \overline{\mu}_H$, and $\overline{\mu}_H + \mathcal{O}(1/T)$ goes to zero as the period goes to $+\infty$, which means that $\overline{\mu}_S$ becomes an accurate approximation for large periods T. In this section, we will provide a lower and upper bounds for $\overline{\mu}_H$ to understand its relation with the speed of the light signal I.

PROPOSITION 3.6. *Let $I : [0, T] \to [0, +\infty)$ be a light signal of class $\mathcal{C}^1$, such that $I_{\min} \leq I(t) \leq I_{\max}$ $\forall t \in [0, T]$. Assuming that all the stationary points of the function $t \mapsto \mu_S(I(t))$ are isolated. For $\{t_i\}_{i=0}^m$ the partition of $[0, T]$, where $t_0 = 0$, $t_m = T$, and $\frac{\mathrm{d}\mu_S(I(t_i))}{\mathrm{d}t} = 0$, then*

$$-\frac{\mu_{\max}}{T} \frac{|\mathcal{I}_-|}{\gamma(I_{\max}) + k_r} \leq \overline{\mu}_H \leq \frac{\mu_{\max}}{T} \frac{|\mathcal{I}_+|}{\gamma(I_{\min}) + k_r},$$

where $|\mathcal{I}_+|$ and $|\mathcal{I}_-|$ are the cardinality of the sets:

$$\mathcal{I}_+ := \left\{ i : \frac{\mathrm{d}\mu_S(I(t))}{\mathrm{d}t} > 0 \ \forall t \in (t_i, t_{i+i}) \right\},$$

$$\mathcal{I}_- := \left\{ i : \frac{\mathrm{d}\mu_S(I(t))}{\mathrm{d}t} < 0 \ \forall t \in (t_i, t_{i+i}) \right\}.$$

Proof. According to the definition of $|\mathcal{I}_+|$ and $|\mathcal{I}_-|$, $\overline{\mu}_H$ can be decomposed into a positive part and a negative part as

$$\overline{\mu}_H = \overline{\mu}_H^+ + \overline{\mu}_H^-,$$

where

$$\overline{\mu}_H^+ := \frac{1}{T} \sum_{i \in \mathcal{I}_+} \int_{t_i}^{t_{i+1}} \frac{\mathrm{d}\mu_S(t)}{\mathrm{d}t} \phi(t) \mathrm{d}t, \quad \overline{\mu}_H^- := \frac{1}{T} \sum_{i \in \mathcal{I}_-} \int_{t_i}^{t_{i+1}} \frac{\mathrm{d}\mu_S(t)}{\mathrm{d}t} \phi(t) \mathrm{d}t.$$

12

Now, we can give an upper bound for the positive part $\overline{\mu}_H^+$ using (3.3)

$$\overline{\mu}_H^+ = \frac{1}{T}\sum_{i\in\mathcal{I}_+}\int_{t_i}^{t_{i+1}}\frac{\mathrm{d}\mu_S(t)}{\mathrm{d}t}\phi(t)\mathrm{d}t,$$

$$\leq \frac{1}{T}\frac{1}{\gamma(I_{\min})+k_r}\sum_{i\in\mathcal{I}_+}\int_{t_i}^{t_{i+1}}\frac{\mathrm{d}\mu_S(t)}{\mathrm{d}t}\mathrm{d}t,$$

$$= \frac{1}{T}\frac{1}{\gamma(I_{\min})+k_r}\sum_{i\in\mathcal{I}_+}\mu_S(t_{i+1})-\mu_S(t_i).$$

In the same way, we can give a lower bound for the negative part using (3.4):

$$\overline{\mu}_H^- = \frac{1}{T}\sum_{i\in\mathcal{I}_-}\int_{t_i}^{t_{i+1}}\frac{\mathrm{d}\mu_S(t)}{\mathrm{d}t}\phi(t)\mathrm{d}t,$$

$$\geq \frac{1}{T}\frac{1}{\gamma(I_{\max})+k_r}\sum_{i\in\mathcal{I}_-}\int_{t_i}^{t_{i+1}}\frac{\mathrm{d}\mu_S(t)}{\mathrm{d}t}\mathrm{d}t,$$

$$= \frac{1}{T}\frac{1}{\gamma(I_{\max})+k_r}\sum_{i\in\mathcal{I}_-}\mu_S(t_{i+1})-\mu_S(t_i).$$

Note that $\overline{\mu}_H^- \leq \overline{\mu}_H \leq \overline{\mu}_H^+$, due to the sign of each term. Then, using the lower bound of $\overline{\mu}_H^-$ and the upper bound of $\overline{\mu}_H^+$, we find:

$$\frac{1}{T}\frac{\sum_{i\in\mathcal{I}_-}\mu_S(t_{i+1})-\mu_S(t_i)}{\gamma(I_{\max})+k_r} \leq \overline{\mu}_H \leq \frac{1}{T}\frac{\sum_{i\in\mathcal{I}_+}\mu_S(t_{i+1})-\mu_S(t_i)}{\gamma(I_{\min})+k_r}.$$

Then, as $\mu_S(t_{i+1})-\mu_S(t_i) \leq \mu_{\max}$, we have

$$-\frac{1}{T}\frac{\sum_{i\in\mathcal{I}_-}\mu_{\max}}{\gamma(I_{\max})+k_r} \leq \overline{\mu}_H \leq \frac{1}{T}\frac{\sum_{i\in\mathcal{I}_+}\mu_{\max}}{\gamma(I_{\min})+k_r}.$$

$\square$

Interpretation of Proposition 3.6 When a particle moves inside a photobioreactor that is constantly mixed, it will not stay in the same position. Therefore, the amount of light perceived I cannot be constant in any interval, and the function $t \mapsto \mu_S(I(t))$ will only have isolated stationary points. The value of $\overline{\mu}_H$ is bounded by the number of times that the derivative of $\mu_S(I(t))$ changes sign. If I is a periodic function as the one analyzed in the Section 3.3, the two sums

$$\sum_{i\in\mathcal{I}_+}\mu(t_{i+1})-\mu(t_i) \text{ and } \sum_{i\in\mathcal{I}_-}\mu(t_{i+1})-\mu(t_i),$$

are independent of T. If $T \to +\infty$, then $\overline{\mu}_H$ converges to 0.

If we could choose the trajectory of a microalgae, we would like to choose the one that can maximize the value of $\overline{\mu}_H$. So, the question is which type of signals provide

13

a higher value of $\overline{\mu}_H$. To give an insight of this, we give a lower bound for $\overline{\mu}_H^+$:

$$\overline{\mu}_H^+ = \frac{1}{T} \sum_{i \in \mathcal{I}_+} \int_{t_i}^{t_{i+1}} \frac{d\mu_S(I(t))}{dt} \int_0^t e^{-\int_s^t \gamma(I(w)) + k_r \, dw} \, dsdt$$

$$\geq \frac{1}{T} \sum_{i \in \mathcal{I}_+} \int_{t_i}^{t_{i+1}} \frac{d\mu_S(I(t))}{dt} \int_0^{t_i} e^{-\int_s^{t_{i+1}} \gamma(I(w)) + k_r \, dw} \, dsdt,$$

$$\geq \frac{1}{T} \sum_{i \in \mathcal{I}_+} \int_{t_i}^{t_{i+1}} \frac{d\mu_S(I(t))}{dt} \int_0^{t_i} e^{-(\gamma(I_{\max})) + k_r)(t_{i+1}-s)} \, dsdt,$$

$$= \frac{1}{T} \sum_{i \in \mathcal{I}_+} \frac{\delta_i}{\gamma(I_{\max}) + k_r} (\mu_S(I(t_{i+1})) - \mu_S(I(t_i))),$$

where $\delta_i = e^{-(\gamma(I_{\max})+k_r)(t_{i+1}-t_i)}(1 - e^{-(\gamma(I_{\max})+k_r)t_i})$.

Increasing the value of $\overline{\mu}_H^+$ will also increases the value of $\overline{\mu}_A$. To increase the value of $\overline{\mu}_H^+$, we can look at the value of $\delta_i(\mu_S(I(t_{i+1})) - \mu_S(I(t_i)))$. The value of δ_i is larger when the time interval (t_i, t_{i+1}) is small. Then, each short interval where the value $\mu_S(I(t_i))$ moves to a higher value $\mu_S(I(t_{i+1}))$ helps to increase the value of $\overline{\mu}_H^+$, and consequently, $\overline{\mu}_A$.

4. Numerical simulations.

4.1. Two periodic examples. For the numerical test, we chose the parameter values of the Han model from [8] as shown in Table 4.1. To illustrate the behavior

Parameter	Value	Unit
k_r	$6.8 \cdot 10^{-3}$	s^{-1}
k_d	$2.99 \cdot 10^{-4}$	-
τ	0.25	s
σ_P	0.047	$m^2 \mu mol^{-1}$
α	$8.7 \cdot 10^{-6}$	-

Table 4.1: Parameter values of the Han model.

of the dynamic growth rate, and specifically to compare it with the static one, we consider two examples of periodic light signals. First, we consider the simple periodic function for the depth of a cell

$$(4.1) \qquad z(t) = \frac{H_0}{2}\left(1 + \sin\left(\frac{2\pi}{T}t\right)\right).$$

The light signal, using the Beer-Lambert law, corresponds to $I(t) = I_0 e^{-\xi z(t)}$ and the static growth rate is $\mu_S(t) = \mu_S(I(t))$. In this case, the value of $\overline{\mu}_S$ is independent of T, by doing the change of variable $s = t/T$, we have

$$\overline{\mu}_S = \frac{1}{T} \int_0^T \mu_S(I(t))dt = \int_0^1 \frac{\alpha\sigma_P I_0 e^{-\xi z(s)}}{1 + \tau\sigma_P I_0 e^{-\xi z(s)} + \frac{k_d}{k_r}\tau\left(\sigma_P I_0 e^{-\xi z(s)}\right)^2} ds.$$

In Figure 4.1a, μ_A is illustrated the periodic solution given by (3.6). As expected, for T large enough, the difference $\overline{\mu}_A - \overline{\mu}_S$ can be approximated by $\overline{\mu}_H$. Numerically, the

14

term $\bar{\mu}_H$, is close to zero. In fact, their relative difference in percentage, computed as $100 \cdot \frac{\bar{\mu}_A - \bar{\mu}_S}{\bar{\mu}_S}$, is lower than 2% as illustrated in Figure 4.1b. As shown in the same figure, $\bar{\mu}_A$ is always greater than $\bar{\mu}_S$ and the difference between them becomes smaller as T increases. When the light dynamics becomes slower, the approximation $\bar{\mu}_A \approx \bar{\mu}_S$ becomes more and more excellent. This property is not always true, as shown in the second example.
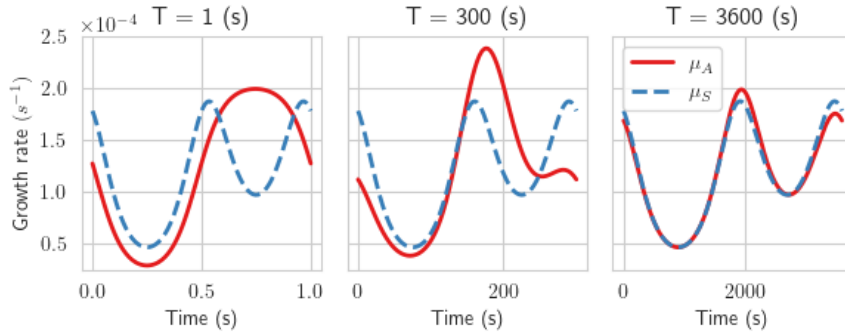
(a) Periodic solution of the dynamic growth rate μ_A (continuous red line) when the light signal is given by the depth following the function (4.1) and the static growth rate (blue dashed line) for three different values of T.
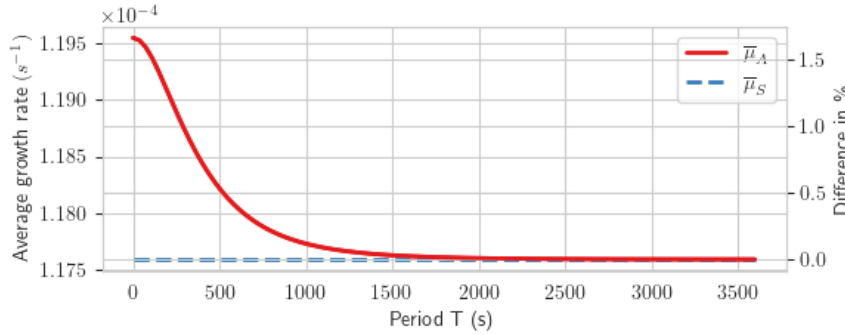
(b) Time-averaged dynamic growth rate (continuous red line) and static growth rate (dashed blue line) for different values of T. The right axis shows the percentage difference.

Fig. 4.1: Dynamic and static growth rate of the light signal taking from Equation (4.1).

For the second example, let us consider the function

(4.2)
$$z(t) = H_0 - 4H_0 \frac{e^{-\left(\sin\left(\frac{2\pi t}{T}\right) - \frac{1}{2}\right)}}{\left(1 + e^{-\left(\sin\left(\frac{2\pi t}{T}\right) - \frac{1}{2}\right)}\right)^2},$$

which has a period T. By doing the same change of variable as above, the time-averaged static growth rate is independent of T. This function describes a movement

15

closer to the surface and does not travel to the deepest part of the culture as in the previous example. Figure 4.2b shows the convergence of $\overline{\mu}_A$ to $\overline{\mu}_S$ as T goes to ∞. The difference between $\overline{\mu}_S$ and $\overline{\mu}_A$ in percentage is higher than the previous case. Also, the value of $\overline{\mu}_A$ is always lower than the value of $\overline{\mu}_S$.

In both examples, μ_A converges to μ_S (see Figure 4.1a and Figure 4.2a). We can see a difference when the value of T is lower than 1500. In this range, we can say that, a strong mixing in the first example promotes growth, where, the second example can represent a poor mixing.
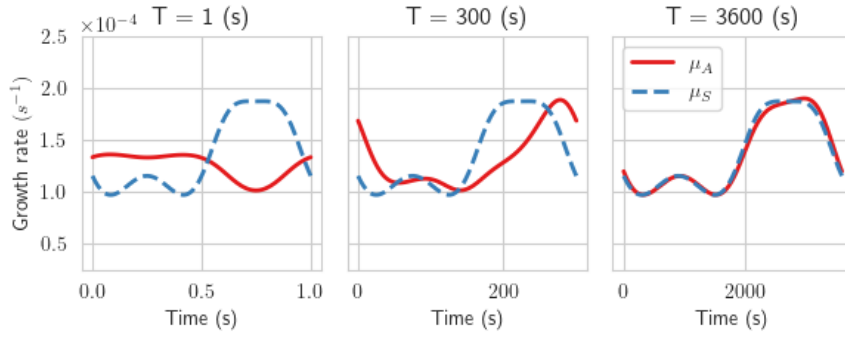
(a) Periodic solution of the dynamic growth rate μ_A (continuous red line) when the light signal is given by the depth following the function (4.2) and the static growth rate (blue dashed line) for three different values of T.
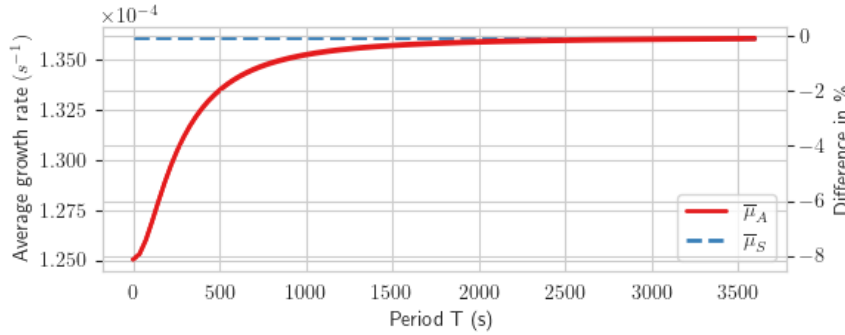
(b) Time-averaged dynamic growth rate (continuous red line) and static growth rate (dashed blue line) for different values of T. The right axis shows the percentage difference.

Fig. 4.2: Dynamic and static growth rate of the trajectory given by Equation (4.2).

4.2. The raceway case. We simulate 8 different conditions by changing the velocity of the paddle wheel for a simulated time of one hour. The initial positions of the particles (x_{n0}, y_{n0}, z_{n0}) are randomly generated following an independent uniform
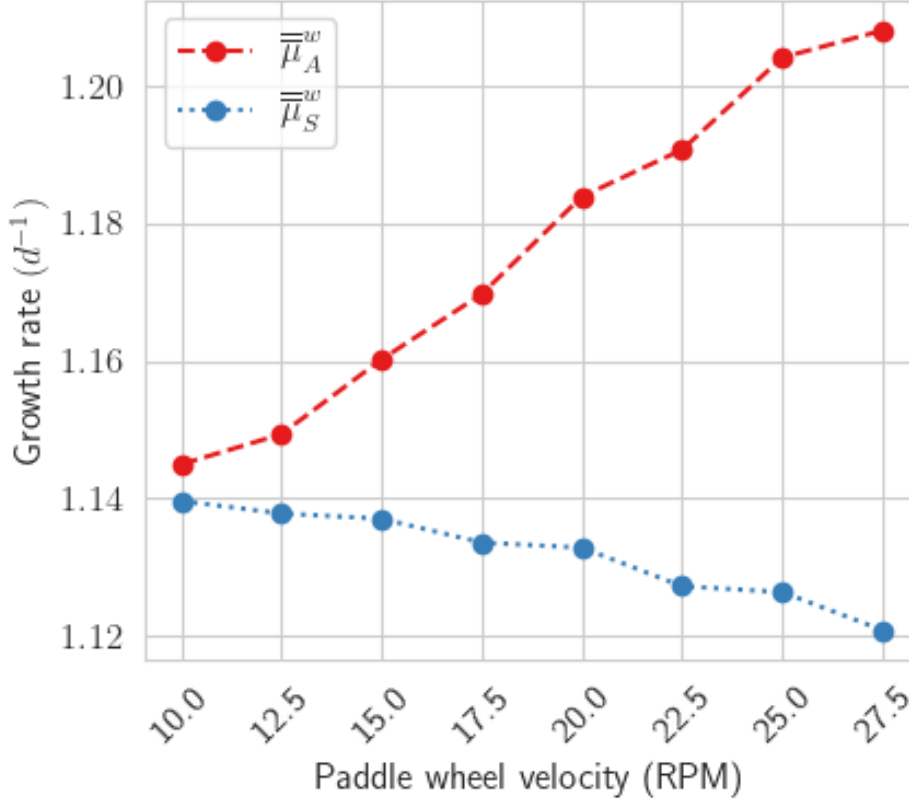
16

Fig. 4.3: For 8 different velocities of the paddle wheel, the estimated space-time-averaged growth rate $\overline{\overline{\mu}}_A^w$ (segmented red line), and the weighted space-time-averaged static growth rate $\overline{\overline{\mu}}_S^w$ (segmented blue line). The hydrodynamics was simulated for 1 hour. The values of N_{par} are different for each simulation, and they are shown in Table 4.2. The average height of the water is $H_0 = 0.3(m)$.

427   distribution $x_{n0} \sim \mathcal{U}_{[x_{\min}, x_{\max}]}$, $y_{n0} \sim \mathcal{U}_{[y_{\min}, y_{\max}]}$, $z_{n0} \sim \mathcal{U}_{[z_{\min}, z_{\max}]}$, where the volume

428 $$B = [x_{\min}, x_{\max}] \times [y_{\min}, y_{\max}] \times [z_{\min}, z_{\max}],$$

429   is such that $\Omega \subset B$, then we ignore the particles outside the domain Ω of the race-
430   way pond. Due to this process, the simulations made have a different number of
431   simulated particles N_{par}. Table 4.2 shows the number of simulated particles for each
432   simulation and also the total time of CPU used. The software Freshkiss3D solve the
433   Equation (2.15) at the same time it tracks the particles solving Equation (2.17). Ex-
434   periments were run on a computer with an Intel Xeon w-2223 processor running at
435   1200 MHz with a total of 15677 MB of RAM, using Fedora version 39.
436   The particles needed to compute $\overline{\overline{\mu}}_A$ and $\overline{\overline{\mu}}_S$ should be representative of the en-
437   tire raceway pond, this means that the distribution should be uniform, at least on
438   the z-axis. At the beginning, the uniform distribution is imposed, but after some

17

time of simulation, due to error accumulation in a periodic domain, the distribution of the particles change. It follows that the space-time-averaged growth rate is not representative anymore. To tackle this problem, more particles could be simulated, but this solution is very CPU demanding and time-consuming. Another approach consists in correcting the particle's distribution at each time, to have a set of particles that permanently represent an actual distribution. The weighted averages can then be defined as:

$$
\overline{\overline{\mu}}_A^w = \frac{1}{T} \int_0^T \frac{\sum_{n=1}^{N_{par}} \frac{\mu_A(I_n(t))}{h(t)}}{\sum_{n=1}^{N_{par}} \frac{1}{h(t)}} \, \mathrm{d}t \quad \text{and} \quad \overline{\overline{\mu}}_S^w = \frac{1}{T} \int_0^T \frac{\sum_{n=1}^{N_{par}} \frac{\mu_S(I_n(t))}{h(t)}}{\sum_{n=1}^{N_{par}} \frac{1}{h(t)}} \, \mathrm{d}t,
$$

for $\overline{\overline{\mu}}_A$ and $\overline{\overline{\mu}}_S$ respectively. Here $h(t)$ is the probability density function of the depth of the particles at the instant t. If the free surface is perfectly flat with depth H_0, we have that $h_n(0) = 1/H_0$ by construction, and we recover the expression (2.20).

RPM	N_{par}	Total simulation time (hrs)
10	3094	714.8
12.5	3057	620.4
15	3064	742.2
17.5	3073	663.1
20	3064	779.3
22.5	3034	695.1
25	3034	810.5
27.5	3048	730.4

Table 4.2: Number of simulated particles and total CPU time simulation for each experience.

Figure 4.3 shows the computation of $\overline{\overline{\mu}}_A^w$, and $\overline{\overline{\mu}}_A^w$. When the particle number N_{par} is large enough, the space-time-averaged static growth rate defined in (2.20) converges to the volume average growth rate in the sense that

$$
(4.3) \qquad \lim_{N_{par} \to \infty} \frac{1}{N_{par}} \sum_{n=1}^{N_{par}} \overline{\mu}_S(I_n) = \overline{\mu}_\Omega,
$$

when the fluid is incompressible [18]. Numerical simulations do not show a noticeable difference in the height of the waves formed on the free surface. As the volume average growth rate depends only on the shape of the photobioreactor, or in the case of the raceway pond, the shape of the free surface and the volume that it defines. Then two raceway ponds with equivalent shape lead to the same average growth rate, which is completely determined by the incident light intensity and the optical depth [14, Theorem 3]. In this sense, the space-time-averaged static growth rate $\overline{\overline{\mu}}_S$ does not take into account the effect of the hydrodynamics. This effect can be seen in Figure 4.3, where the corrected average have a small variation (1.1395 d^{-1} for 10 RPM and 1.12080 d^{-1} for 27.5 PRM).

5. Conclusions. We present a numerical method to calculate the average growth rate in a photobioreactor, accounting for hydrodynamics. The starting point is the Han model, which takes into account the light history of the microalgae, the Han

18

model coupled with the hydrodynamics can capture the influence of the mixing device. To better understand the effect that mixing can have on growth, we illustrate with two simple periodic functions; the first one increases the actual growth rate compared to the static value, and the second one shows the opposite trend.

We implement the light harvesting model in the light field generated by the hydrodynamics of raceway pond. Since the computational cost is very high for simulating reactor hydrodynamics and tracking the particles to compute the average growth rate, we present an alternative way to compute this growth rate, correcting the distribution in the depth of the particles to have a better representation of the raceway pond.

The computations made in the case of the raceway can be adjusted to other types of reactors. For example, the relationship between the dynamic growth rate and the velocity in the z-axis of the raceway can be transposed to other photobioreactors, depending on the distribution of the light inside the reactor. It can even be used to optimize the reactor geometry, to better benefit from this dynamical effect.

Not all models are able to capture the effect of hydrodynamics, and extending a model to do so it is not straightforward. In this study, we propose a way to take into account the hydrodynamics where we conclude that a better mixing of the photobioreactor, in the raceway pond case, increases the productivity of the photobioreactor. The answer to whether or not hydrodynamics should be considered among the factors affecting microalgae growth has no single answer, since it will depend on the geometry of the photobioreactor and the light distribution inside it. However, in this paper, we present upper and lower bounds of the growth function that may be useful in determining when hydrodynamics should be considered.

REFERENCES

[1] ALI, H., CHEEMA, T. A., YOON, H.-S., DO, Y., AND PARK, C. W. Numerical prediction of algae cell mixing feature in raceway ponds using particle tracing methods. *Biotechnology and bioengineering 112*, 2 (2015), 297–307.

[2] ALLGEYER, S., BRISTEAU, M.-O., FROGER, D., HAMOUDA, R., JAUZEIN, V., MANGENEY, A., SAINTE-MARIE, J., SOUILLÉ, F., AND VALLÉE, M. Numerical approximation of the 3D hydrostatic Navier–Stokes system with free surface. *ESAIM: Mathematical Modelling and Numerical Analysis 53*, 6 (2019), 1981–2024.

[3] BÉCHET, Q., SHILTON, A., AND GUIEYSSE, B. Modeling the effects of light and temperature on algae growth: state of the art and critical assessment for productivity prediction during outdoor cultivation. *Biotechnology advances 31*, 8 (2013), 1648–1663.

[4] BERNARD, O., BOULANGER, A.-C., BRISTEAU, M.-O., AND SAINTE-MARIE, J. A 2D model for hydrodynamics and biology coupling applied to algae growth simulations. *ESAIM: Mathematical Modelling and Numerical Analysis 47*, 5 (2013), 1387–1412.

[5] BERNARD, O., MAIRET, F., AND CHACHUAT, B. Modelling of microalgae culture systems with applications to control and optimization. *Microalgae Biotechnology* (2015), 59–87.

[6] EILERS, P., AND PEETERS, J. A model for the relationship between light intensity and the rate of photosynthesis in phytoplankton. *Ecological modelling 42*, 3-4 (1988), 199–215.

[7] FIERRO ULLOA, J. I., LU, L.-D., AND BERNARD, O. Theoretical growth rate of microalgae under high/low-flashing light. *Journal of Mathematical Biology 86*, 4 (2023), 48.

[8] GRENIER, J., LOPES, F., BONNEFOND, H., AND BERNARD, O. Worldwide perspectives of rotating algal biofilm up-scaling. Submitted paper, 2020.

[9] HAN, B.-P. A mechanistic model of algal photoinhibition induced by photodamage to photosystem-II. *Journal of theoretical biology 214*, 4 (2002), 519–527.

[10] HARTMANN, P., BÉCHET, Q., AND BERNARD, O. The effect of photosynthesis time scales on microalgae productivity. *Bioprocess and biosystems engineering 37*, 1 (2014), 17–25.

[11] HARTMANN, P., DEMORY, D., COMBE, C., HAMOUDA, R., BOULANGER, A.-C., BRISTEAU, M.-O., SAINTE-MARIE, J., SIALVE, B., STEYER, J.-P., RABOUILLE, S., ET AL. Growth rate estimation of algae in raceway ponds: A novel approach. *IFAC Proceedings Volumes 47*, 3 (2014), 6216–6221.

[12] HREIZ, R., SIALVE, B., MORCHAIN, J., ESCUDIÉ, R., STEYER, J.-P., AND GUIRAUD, P. Ex-

perimental and numerical investigation of hydrodynamics in raceway reactors used for algaculture. *Chemical Engineering Journal 250* (2014), 230–239.

[13] KHALIL, H. *Nonlinear Systems*. Pearson Education. Prentice Hall, 2002.

[14] MARTÍNEZ, C., MAIRET, F., AND BERNARD, O. Theory of turbid microalgae cultures. *Journal of theoretical biology 456* (2018), 190–200.

[15] NIKOLAOU, A., BOOTH, P., GORDON, F., YANG, J., MATAR, O., AND CHACHUAT, B. Multi-physics modeling of light-limited microalgae growth in raceway ponds. *IFAC-PapersOnLine 49*, 26 (2016), 324–329.

[16] PANDEY, R., AND PREMALATHA, M. Design and analysis of flow velocity distribution inside a raceway pond using computational fluid dynamics. *Bioprocess and Biosystems engineering 40*, 3 (2017), 439–450.

[17] PRUSSI, M., BUFFI, M., CASINI, D., CHIARAMONTI, D., MARTELLI, F., CARNEVALE, M., TREDICI, M. R., AND RODOLFI, L. Experimental and numerical investigations of mixing in raceway ponds for algae cultivation. *Biomass and bioenergy 67* (2014), 390–400.

[18] TONG, Z.-X., LI, M.-J., YAN, J.-J., AND GU, Z.-L. A theoretical analysis of the hydrodynamic influence on the growth of microalgae in the photobioreactors with simple growth kinetics. *International Journal of Heat and Mass Transfer 158* (2020), 119986.

20